

Albedo Reduction by Black Carbon in Snow: Measurements and Implications

Charles S. Zender^{1,2}, Jean-Charles Gallet¹, Florent Dominé¹, Ghislain Picard¹, and Mark G. Flanner³

¹Laboratoire de Glaciologie et Géophysique de l'Environnement, Grenoble, France

²Department of Earth System Science, University of California, Irvine

³National Center for Atmospheric Research, Boulder, Colorado

Department of Earth System Science
University of California, Irvine
Irvine, CA 92697-3100

zender@uci.edu
Voice: (949) 824-2987
Fax: (949) 824-3256

Abstract

Industrial and biomass burning emissions of black carbon (BC) from low- and mid-latitudes dominate the radiative forcing by absorbing impurities trapped in snow and ice at mid- and high- northern latitudes. Correct model representation of albedo reduction by BC-contaminated snow is crucial because our GCM simulations show that dirty snow can explain about 30% of the observed 20th century Arctic warming. Until now, measurements of actual snow darkening by BC have been attempted only in the field, under non-reproducible conditions, and limited by the BC concentration that happens to be present.

We have conducted the first measurements of the direct effect of BC-contamination on snow albedo by in a controlled environment. We doped natural snow with a commercially available BC-analogue and measured the resulting albedo change at visible and near-infrared wavelengths. Snow albedo was measured in a (portable) integrating sphere system. Snow grain size is estimated from the near-infrared albedo. Snow density, temperature, and BC properties were known a priori. The albedo measurement reproducibility is about 1% for natural snow.

Our measurements agree with model predictions that BC concentrations from 250 ppb to 200 ppm darken visible snow albedo by 1–70%. This experimental confirmation of the modeled albedo reduction has limits: First, BC contamination of polar snow and ice is typically < 30 ppb, an order of magnitude smaller than our albedo sensitivity. Second, horizontal and vertical “edge effects” in our measurement system produce visible albedos that differ from semi-infinite, plane-parallel geometries by about 50%. Finally, BC deposited in polar regions may be aged, hygroscopically coated, and/or internally mixed with snow grains. Hence our results are an early step toward evaluating and improving model representation of BC effects in the complex cryosphere. Moreover, the fast, lightweight system makes possible in situ measurements of snow albedo in remote locations during IPY.

1 Introduction

Light-absorbing impurities including black carbon (BC) and dust reduce snow and ice reflectivity (Warren and Wiscombe, 1980; Chylek et al., 1983) and can thereby trigger ice-albedo feedbacks

28 (*Warren, 1984*, e.g.,). If our representation of the associated processes in climate models is ade-
29 quate, then snow-darkening by anthropogenic BC deposition is a major contributor to recent Arctic
30 warming (*Hansen and Nazarenko, 2004; Jacobson, 2004; Flanner et al., 2007; Quinn et al., 2008*).
31 Here we report the first laboratory measurements of the direct effect of BC-contamination on snow
32 albedo in a controlled environment.

33 BC darkens snow and alters climate through a series of processes that climate models ap-
34 proximate with varying degrees of uncertainty. The fundamental cause of snow darkening is the
35 contrast between the single scattering albedo of BC, the darkest aerosol, and that of snow, the
36 brightest surface. These single scatter albedos depend, respectively, on the chemical composi-
37 tion, structure, and mixing state of BC (*Bond and Bergstrom, 2005*), and on the size and shape
38 of snow crystals (*Warren and Wiscombe, 1980; Grenfell and Warren, 1999*). Models show that
39 15 ppbm (parts-per-billion-by-mass) of BC externally mixed in snow of optically-equivalent effec-
40 tive radius $r_e = 100\mu\text{m}$ will darken the snow albedo by about 1% at the mid-visible wavelength
41 $\lambda = 500\text{ nm}$ (*Grenfell et al., 1994*).

42 Many recent regional-to-global studies follow the approach to estimating BC-perturbation of
43 snow albedo outlined by *Warren and Wiscombe (1980)*. *Flanner et al. (2007)* represent aspherical
44 effects through the specific-surface-area (*Grenfell and Warren, 1999*, e.g.,). *Flanner et al. (2007)*
45 account for aspherical effects by prognosing SSA (or, equivalently, effective radius) instead of
46 number size distribution. *Jacobson (2004)* and *Flanner et al. (2007)* both account for coated BC.
47 *Hansen and Nazarenko (2004) Jacobson (2004) Krinner et al. (2006) Flanner et al. (2007) ?*

48 *Flanner et al. (2007)* analyzed five sources of uncertainty that affect the instantaneous surface
49 radiative forcing ΔF_R^{sfic} caused by BC impurities in snow. The fxm, in decreasing order of impor-
50 tance to ΔF_R^{sfic} , were 1. BC emission strength (i.e., total amount available to darken snow), 2. Snow
51 aging (affects snow crystal size and thus reflectivity), 3. Melt scavenging (residence time of BC in
52 snowpack), 4. BC optical properties, and 5. snow cover fraction (land fraction covered by given
53 snow thickness). Although these sensitivity tests were formulated subjectively, the results indicate
54 how robust

55 At least two previous measurement techniques have been employed to estimate the albedo
56 perturbation of BC in snow. First, the near-infrared (NIR) albedo of snow is not sensitive to small
57 impurity concentrations and is therefore used to constrain the optically equivalent snow grain size
58 in a snow radiative transfer model (*Warren and Clarke, 1990*). NIR-reflectance techniques have
59 been used with spectrometers to perform rapid snow pack stratigraphy in the field (*Painter et al.,*
60 *2007*). The hypothetical albedo of pure snow is then estimated (*Warren, 1982*) using the NIR-
61 determined snow grain size, and is compared to the measured visible albedo of BC-contaminated
62 snow. Additional analysis (e.g., minimized residuals of spectral mixtures) can help segregate the
63 effects of BC from other known contaminants such as dust (*Warren and Clarke, 1990*).

64 The second method for estimating the albedo perturbation by BC requires laboratory facilities.
65 Collected snow samples are melted and filtered. Filters are then analyzed using thermo-optical
66 techniques to measure elemental carbon, organic, or total carbon (?), or by pure optical techniques
67 previously calibrated against standard soot absorptance (*Noone and Clarke, 1988*). The latter
68 method yields a BC concentration which is self-consistent with the assumed optical properties.
69 This concentration may then be used to estimate the (and/or compare to the field-measured) snow
70 albedo.

71 The commonality of these previous studies is that the contaminant mass is *a priori* unknown.
72 Our experiments test the albedo perturbation of a known mass of BC. We dope natural snow with

73 pre-measured quantities of BC in order to assess the adequacy of snow radiative transfer models at
74 reproducing observed albedo perturbation over orders of magnitude of BC mass.

- 75 1. rdsffc effective radius *Munneke et al. (2008)*
- 76 2. ryt ray-tracing *Picard et al. (2008)*

77 **2 Methods**

78 Our procedure measure the perturbation to snow albedo by BC followed these steps:

- 79 1. Collect fresh surface snow
- 80 2. Weigh BC
- 81 3. Weigh snow
- 82 4. Separately blend control and BC-doped snow samples
- 83 5. Dilute snow samples as necessary
- 84 6. Measure snow density
- 85 7. Measure 1310 nm-reflectance
- 86 8. Measure 630 nm-reflectance

87 We collected surface snow for these experiments during short expeditions to nearby Chamrousse
88 Ski Station (elevation ~ 1750 m). To minimize accumulation of impurities, all specimen collection
89 took place within 24-hours of snowfalls lasting at least 24-hours. Any impurities present in the
90 fresh snow samples contribute to excess absorption in both the clean and doped snow experiments
91 described below.

92 Prior to collection we measured *in situ* properties (air and snow temperature, snow density and
93 stratigraphy). Near surface air temperature never exceeded $T = -0.5^\circ\text{C}$ between snowfall and
94 collection. Surface specimens (top ~ 50 cm) were transported to LGGE. All subsequent handling,
95 preparation, and measurement of snow took place in a constant-temperature (-15°C) cold-room
96 facility at LGGE.

97 We doped snow with commercially available Monarch 120 Carbon Black supplied by Cabot
98 Corporation (Billerica, MA, USA). Monarch 120 is most similar to the discontinued product
99 Monarch 71 used to calibrate optically effective BC concentration in many previous studies (e.g.,
100 *Clarke and Noone, 1985; Warren and Clarke, 1990; Clarke et al., 2004*) (S. Warren, personal com-
101 munication, 2007). Monarch 120 is not, strictly speaking, soot (*Watson and Valberg, 2001*), nor
102 is it pure elemental carbon (EC). Monarch 120 is our experimental analogue for light-absorbing
103 carbon (*Bond and Bergstrom, 2005*) aerosol in the climate system, and we refer to it simply as BC
104 henceforth.

105 BC samples of 3–100 mg were weighed on a precision scale, then mixed into the snow spec-
106 imens of approximately 440 g. Mixing was accomplished with a commercially available blender
107 composed of aluminum and stainless steel. Blending for one minute, adding BC, then blending for
108 2.5 minutes produced darkened snow that appeared homogeneous. This mixing procedure created
109 doped snow with initial BC mixing ratios $7.5 \leq m_{mr}BC \leq 221$ ppmm. Some of this material
110 was diluted with clean snow in the blender to obtain BC mixing ratios as low as $q_{BC} = 250$ ppbm.
111 One minute of additional blending was performed per dilution stage.

112 Blank snow specimens were created with the same procedure, but without adding BC. To pre-
113 vent contamination, separate sets of mixing elements were maintained for the blanks and doped
114 samples. All components were washed in 18 M Ω -cm water between uses, and no residual BC was
115 noticed on the mixing elements.

116 The key optical measurements were made with the integrating sphere described in *Gallet et al.*
117 (2008), hereafter GDZ09. Collimated radiation from diode lasers strikes a snow sample flush with
118 the sphere bottom. After multiple scattering, the diffuse radiation striking an InGaAs photodiode
119 is converted to a voltage. The photodiode sits behind an optical baffle to screen-out specular reflec-
120 tion. The voltage-to-reflectance conversion is calibrated by measurements of reflectance standards
121 (Sphere Optics Inc.) made before and after snow sample measurement.

122 Our experiments used two diode-lasers (635 and 1310 nm) so we could measure the visible
123 and NIR snow albedos, A_{635} and A_{1310} , respectively. Hence we refer to this system as DUFISS,
124 the DUal-Frequency Integrating Sphere for Snow. GDZ09 describe more fully the geometric and
125 optical properties of DUFISS.

126 2.1 Models

127 Snow reflectance is primarily determined by its specific surface area (SSA), the surface-area-to-
128 mass ratio (*Grenfell and Warren, 1999*). SSA is inversely related to the optically effective snow
129 grain size, aka effective radius r_e . Snow NIR reflectance is highly correlated with SSA (*Domine*
130 *et al., 2006*), and is insensitive to small amounts of impurities. GDZ09 describe how we calibrate
131 1310 nm reflectance A_{1310} to SSA measured by methane adsorption techniques.

132 Snow albedo simulations were performed with the Shortwave Narrow Band (SWNB2) radiative
133 transfer model *Zender et al. (1997)*; *Zender (1999)*; *Zender and Talamantes (2006)*. SWNB2
134 solves for all radiant quantities at 10 cm⁻¹ spectral resolution from 0.2–5.0 μ m using the discrete
135 ordinates technique (*Stamnes et al., 1988*). Ice refractive indices at 635 and 1310 nm values are
136 as in *Warren and Brandt (2008)*. Snow samples were treated as plane-parallel and homogeneous
137 (constant density with depth). Edge effects are discussed below.

138 Model inputs include the snow density (measured), snow SSA (estimated from 1310 nm re-
139 flectance as in GDZ09), and the geometric standard deviation σ_g of the snow grain size distribu-
140 tion. *Grenfell and Warren (1999)* found $\sigma_g = 1.6$ is typical at the South Pole, and *Flanner and*
141 *Zender (2006)* showed $\sigma_g = 2.3$ best fits observed grain-size evolution for young snow, and *Gallet*
142 *et al. (2008)* found $\sigma_g = 1.4$ best matches reflectance measurements at $\lambda = 1550$ nm. The modeled
143 reflectance for $\sigma_g = 2.3$ is greater than that for $\sigma_g = 1.4$ by about 0.8% and 1.1% for $\lambda = 635$ and
144 1310 nm, respectively. This study uses $\sigma_g = 2.3$ for consistency with the SNICAR model.

145 Our treatment of BC optical properties is identical to *Flanner et al. (2007)*. Spectral variation of
146 the BC refractive index is from *Chang and Charalampopoulos (1990)*. A lognormal BC size distri-
147 bution is assumed with number-median radius 50 nm and geometric standard deviation $\sigma_g = 1.5$.
148 Tuning the BC density to 1322 kg m⁻³ leads to a mass absorption coefficient $\psi = 7500$ m² kg⁻¹ at
149 $\lambda = 550$ nm, in agreement with the central estimate of *Bond and Bergstrom (2005)*. We perform
150 sensitivity studies to the effects of sulfate coatings on BC. These coatings increase the mass ab-
151 sorption coefficient relative to uncoated BC of the same mass by a factor of about 1.6 (*Bond et al.,*
152 *2006*).

Table 1: Measurements

BC	λ	N	ID
0.0 ppbm	635	5	20071211c
0.0 ppbm	635	5	20071210d
0.0 ppbm	1310	3	20071211d
0.0 ppbm	635	10	20080130b
0.0 ppbm	1310	3	20080130e
250 ppbm	635	10	20080131a
250 ppbm	1310	3	20080131c
750 ppbm	635	10	20080130h
750 ppbm	1310	3	20080130g
1.5 ppmm	635	10	20071211a
1.5 ppmm	1310	3	20071211f
7.5 ppmm	635	10	20080130a
7.5 ppmm	1310	3	20080130f
16 ppmm	635	10	20071210f
16 ppmm	1310	3	20071210c
221 ppmm	635	5	20071206e
221 ppmm	1310	1	20071207d

153 **2.2 Edge Effects**

154 Boundary conditions include the snow sample depth (25 mm), and sample-holder reflectance (0.06).

155 **2.3 Measurements**

156 We report here reflectance measurements from $N = 97$ individual snow samples (summarized in
157 Table 1). Samples were either clean (not doped) or doped with one of six BC mixing ratios q_{BC}
158 between 250 ppbm and 221 ppmm. The darkest doped snow ($q_{BC} = 221$ ppmm) has These three
159 orders of magnitude of BC concentration do not overlap

160 **3 Results**

161 Wow!

162 **4 Discussion**

163 Our measurements suggest that BC perturbs visible albedo by less than some earlier studies. ?
164 state that 100 ppmm BC reduces albedo at $0.5 \mu\text{m}$ from 0.95 to 0.1, based on a polynomial fit to
165 Figure 1c of *Jacobson (2004)*. Our experiments suggest 100 ppmm a reduction of f_{xm} to f_{xm} .
166 These discrepancies are likely explicable in terms of differences in the assumed BC refractive
167 index.

168 **5 Conclusions**

169 Clean snow:

- 170 • Using specific surface area (inferred from 1310 nm reflectance) improves visible snow albedo
171 predictions (at 635 nm)

172 Dirty snow:

- 173 • First controlled measurements of snow darkening by impurities
174 • Albedo within $\sim 1\%$ of predictions from 250 ppm to 250 ppb
175 • Closer agreement with externally mixed uncoated BC than with externally mixed sulfate-
176 coated BC

177 LGGE Integrating Sphere for Snow Albedo:

- 178 • Natural snow variability limits measurement reproducibility to albedo changes of $\sim 1\%$
179 (~ 250 ppb BC)
180 • Portability makes possible in situ snow albedo measurements for, e.g., cal/val of satellite-
181 retrieved snow SSA/albedo

Measured + Modeled Snow Albedo

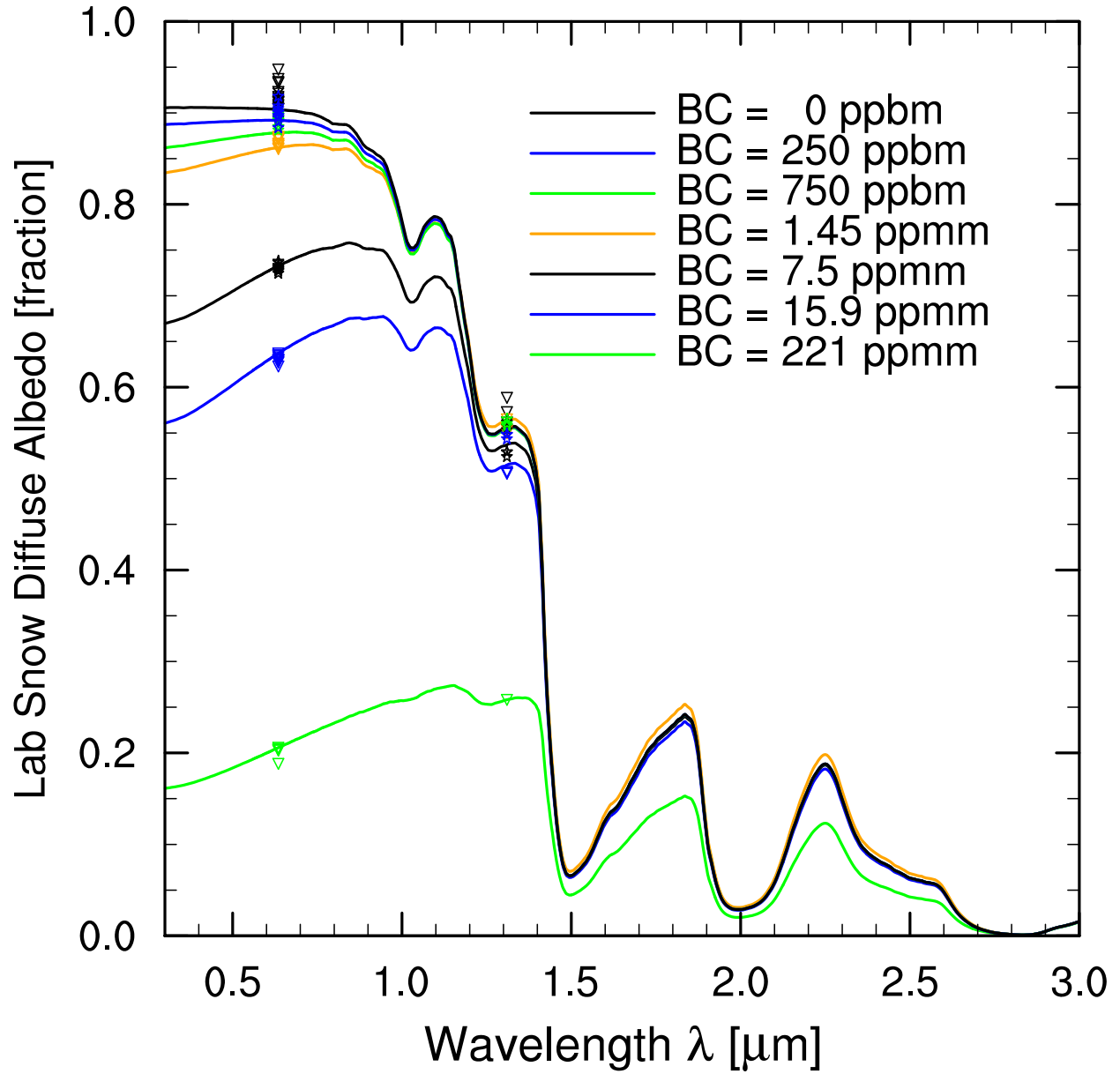


Figure 1: Measured and modeled snowpack reflectance for varying soot (BC) concentration.

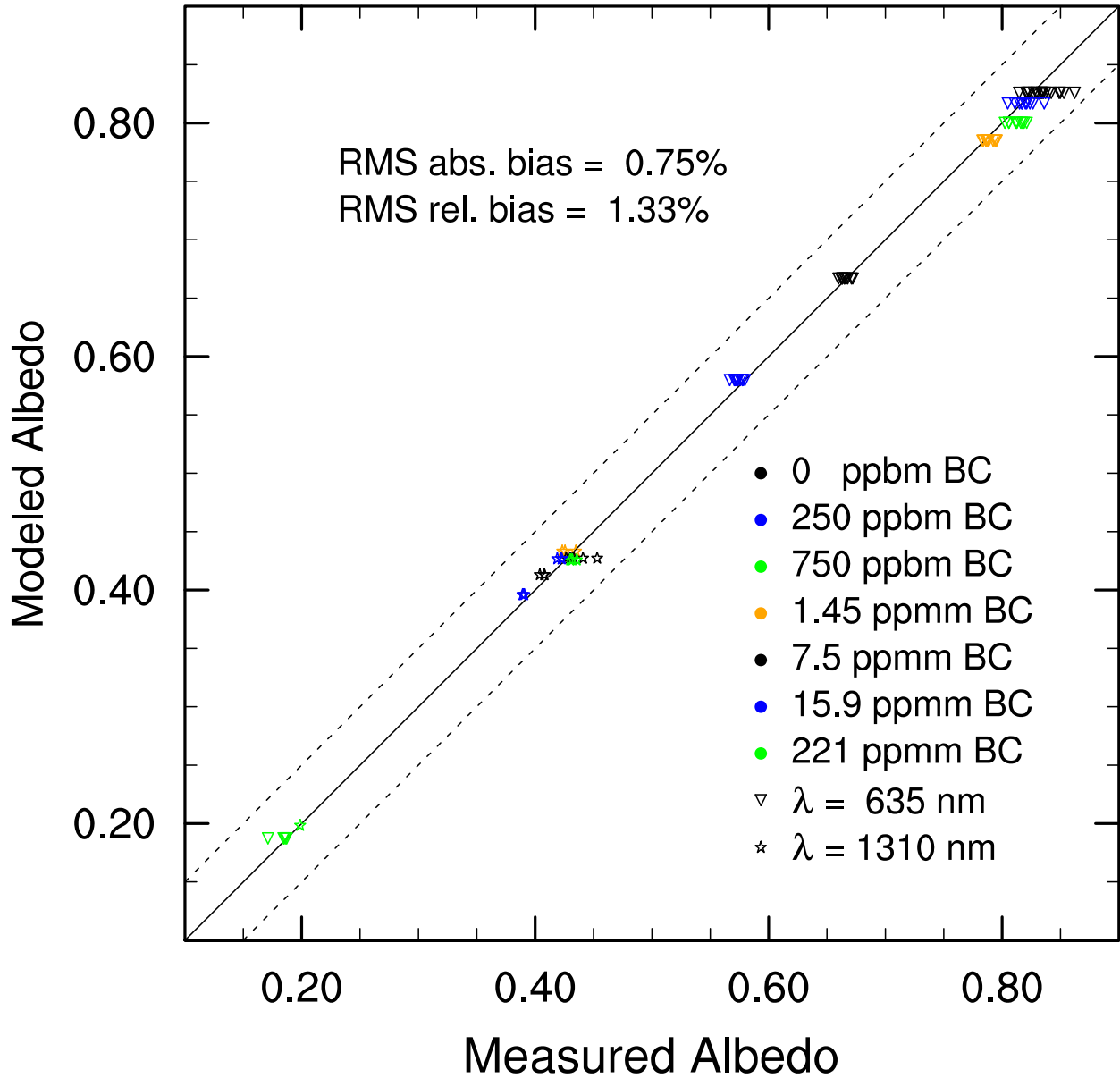


Figure 2: Measured vs. modeled snowpack reflectance for varying soot (BC) concentration. Estimated SSA.

6 Integrating Spheres

An “ideal” integrating sphere would differ from our apparatus in at least three ways:

1. Its large aperture would eliminate horizontal boundary effects caused by the sample holder walls. The plane-parallel geometry would allow snow of all depths, not just surface snow, to “see” the sphere as an hemispheric (2π sr) aperture.
2. Its deep sample-holder would always appear “semi-infinite” (*Wiscombe and Warren, 1980*), i.e., the sample holder bottom would contribute negligibly to surface albedo measurements.
3. The cavity would be perfectly spherical and reflective, with negligible surface area devoted to optical probes, baffles, and sensors.

Our measurements can be affected by both these issues, so we simulate their impact using geometrical and optical reasoning. Three ways in which the measurements deviate from those expected from an “ideal” apparatus can be The finite aperture of the integrating sphere reduces the solid angle subtended by sub-surface snow. Moreover, light snow allows incident radiation to penetrate to and be absorbed by the sample holder bottom (albedo= 0.06).

This fraction is strongly wavelength dependent. penetrate through the sample and to absorbed by the sample holder.

6.1 Geometry

Consider an integrating sphere of radius R_{IS} that has an aperture of radius R_s at the bottom (Figure ??). Beneath the aperture is a sample cylinder of radius $R_e \geq R_s$ and thickness z_e . The sample cylinder is full of snow whose exposed surface is approximately tangent to the integrating sphere. Snow at radius r from the center and depth z from the surface subtends an angle $\psi(r, \phi, z; R_s)$ within the sphere. Here ϕ is the azimuthal angle in the plane of the sample. The semi-colon separates dependence on continuous, integrable variables (r, ϕ, z) from dependence on fixed parameters (R_s) .

During fabrication of the integrating sphere, the finite “lip” between the sphere and the sample holder was beveled and reflectively coated to ensure that upwelling radiation that impinges on the lip is directed into the sphere. Thus surface snow has $\psi(r, \phi, 0; R_s) \approx \pi$. Some light up-scattered from sub-surface snow misses the aperture and falls within the geometric shadow of the sample holder walls. The planar angles ψ_1 and ψ_2 subtend the “shadowed” portion of the hemisphere from the walls to the bottom of the integrating sphere. These angles supplement ψ such that

$$\begin{aligned}\psi_1 + \psi + \psi_2 &= \pi \\ \psi &= \pi - (\psi_1 + \psi_2)\end{aligned}\tag{1}$$

Trigonometric relationships link the planar angles to the integrating sphere and sample-holder geometry. The relationship depends on the on the lengths of circular chords that pass through the point. The radial distance r from the center and the azimuthal angle ϕ of the chord together determine how “off-center” each point sits along a given chord. Points centered on the chord have $\psi_1 = \psi_2$, and all other points cut the chord into two uneven pieces. The planar angles (1) follow immediately as the arctangent of the sample depth divided by the partial chord lengths.

The circular symmetry of the sample and integrating sphere allow us to imagine each small element of snow as laying on the x -axis. The azimuthal direction $\phi = 0$ is parallel to the y -axis and fixes the “north” end of the sample in the sample plane. First consider the planar angles subtended by the sample for $\phi = \pi/2$, i.e., angles in the plane which contains the x -axis. This plane also contains the origin and creates chords, therefore, that are also diameters of the sample aperture. Each chord (diameter) has length $2R_s$. Points on these chords are distances $R_s - r$ and $R_s + r$ from the near and far edges of the aperture, respectively. The planar angles subtended from depth z are

$$\psi_1(r, \phi = \pi/2, z; R_s) = \arctan\left(\frac{z}{R_s - r}\right) \quad (2a)$$

$$\psi_2(r, \phi = \pi/2, z; R_s) = \arctan\left(\frac{z}{R_s + r}\right) \quad (2b)$$

Next consider the planar angles subtended by the sample for $\phi = 0$, i.e., angles in the plane which is parallel to the y -axis. Points bisect these chords into two equal segments. The chords are not diameters so the segments are not radii as in (2). Each segment forms a right triangle with hypotenuse length R_s and other side length r . The Pythagorean theorem establishes the length of each half-chord as $\sqrt{R_s^2 - r^2}$. The planar angles subtended from depth z are, therefore,

$$\psi_1(r, \phi = 0, z; R_s) = \psi_2(r, \phi = 0, z; R_s) = \arctan\left(\frac{z}{\sqrt{R_s^2 - r^2}}\right) \quad (3)$$

The above procedure extends to the planar angles subtended by arbitrary azimuthal angles. In general, the chord segments are not diameters (2), nor are they equal in length (3). Instead, points cut their chords a distance $r \sin \phi$ from the bisection (chord-center) point, and form unequal chord segments. This displacement from chord-center is one side of a right triangle with hypotenuse r . The other side, of length $r \cos \phi$, is the distance of the bisection point from the sample center. A bisected chord at azimuthal angle ϕ , therefore, is length $\sqrt{R_s^2 - r^2 \cos^2 \phi}$. This length, adjusted by the displacement of the snow element from chord center, gives the distances of the snow element to the edges of the sample holder along the azimuthal angle ϕ . The planar angles follow directly from these chord segment lengths and the snow depth,

$$\psi_1(r, \phi, z; R_s) = \arctan\left(\frac{z}{\sqrt{R_s^2 - r^2 \cos^2 \phi} - r \sin \phi}\right) \quad (4a)$$

$$\psi_2(r, \phi, z; R_s) = \arctan\left(\frac{z}{\sqrt{R_s^2 - r^2 \cos^2 \phi} + r \sin \phi}\right) \quad (4b)$$

212 One can see that (4) reduces to (2) and (3) for $\phi = \pi/2$ and $\phi = 0$, respectively.

Circular symmetry of the sample aperture leads to multiple symmetries in the planar angles. First, the supplementary angles are mirror symmetric about $\phi = 0$. Substituting $-\phi$ for ϕ in (4):

$$\psi_1(r, \phi, z; R_s) = \psi_2(r, -\phi, z; R_s) \quad (5a)$$

$$\psi_2(r, \phi, z; R_s) = \psi_1(r, -\phi, z; R_s) \quad (5b)$$

$$\psi(r, \phi, z; R_s) = \psi(r, -\phi, z; R_s) \quad (5c)$$

The third relation follows from using (5a) and (5b) in (1). Similarly, the planar angles are symmetric under rotation by π :

$$\psi_1(r, \phi, z; R_s) = \psi_2(r, \phi + \pi, z; R_s) \quad (6a)$$

$$\psi_2(r, \phi, z; R_s) = \psi_1(r, \phi + \pi, z; R_s) \quad (6b)$$

$$\psi(r, \phi, z; R_s) = \psi(r, \phi + \pi, z; R_s) \quad (6c)$$

213 The third relation follows from using (6a) and (6b) in (1).

We are interested in the field-of-view (FOV) within the integrating sphere seen by a snow element in the sample holder. The mean planar angle $\bar{\psi}$ of the spherical cavity seen by each snow element is the planar (i.e., two-dimensional) FOV of the point. By definition,

$$\bar{\psi}(r, z; R_s) \equiv \frac{2}{\pi} \int_0^{\pi/2} \psi(r, \phi, z; R_s) d\phi \quad (7)$$

214 That evaluating ψ only over a quarter-circular domain, i.e., $0 < \phi < \pi/2$, suffices to determine its
215 azimuthal-mean follows from (5c) and (6c).

The full, three-dimensional FOV of each snow element is proportional to the area of the integrating sphere seen by the point. Rotating the mean planar angle $\bar{\psi}$ (7) about the vertical axis z yields the solid angle Ω of integrating sphere seen by a single snow element:

$$\Omega(r, z; R_s) = 2\pi \left(1 - \cos \frac{\bar{\psi}(r, z; R_s)}{2} \right) \quad (8)$$

216 Note that this FOV is purely a geometric measure and thus correction. Radiative transfer is required
217 to account for the transmission and scattering by overlying snow.

218 The local solid angle Ω depends on $\cos(\bar{\psi})$ (8), a non-linear function of r . Hence (9) differs
219 from the solid angle which would be obtained by rotating (8) the areal-mean planar angle (10).

To correct the albedo contribution from sub-surface snow for the effects of reduced aperture at depth, we need the areal-mean FOV of all snow at a given depth, i.e., the areal-mean of (8). Assuming that the sample is uniformly illuminated within a circle of radius $R \leq R_s$, then the area-weighted value of Ω across the illuminated area is:

$$\begin{aligned} \bar{\Omega}(z; R_s, R) &\equiv \frac{1}{\pi R^2} \int_0^R 2\pi r \Omega(r, z; R_s) dr \\ &= \frac{2}{R^2} \int_0^R r \left[2\pi \left(1 - \cos \frac{\bar{\psi}(r, z; R_s)}{2} \right) \right] dr \\ &= 2\pi \left[1 - \frac{2}{R^2} \int_0^R r \cos \frac{\bar{\psi}(r, z; R_s)}{2} dr \right] \end{aligned} \quad (9)$$

220 With the assumption that up-scattered radiation is isotropic, and neglecting other considerations
221 such as multiple scattering, the geometric FOV reduces the albedo contribution of depth z snow by
222 $\bar{\Omega}(z)/(2\pi)$ relative to its contribution in an ideal detector with $\text{FOV} = 2\pi$.

The areal-mean planar angle $\bar{\psi}$ of the spherical cavity seen by all snow at a given depth is also of interest.

$$\begin{aligned}
\bar{\psi}(z; R_s, R) &\equiv \frac{1}{\pi R^2} \int_0^R 2\pi r \bar{\psi}(r, z; R_s) dr \\
&= \frac{2}{R^2} \int_0^R r \left(\frac{2}{\pi} \int_0^{\pi/2} \psi(r, \phi, z; R_s) d\phi \right) dr \\
&= \frac{4}{\pi R^2} \int_0^R \int_0^{\pi/2} r \psi(r, \phi, z; R_s) d\phi dr
\end{aligned} \tag{10}$$

Unfortunately, the complex form of the planar angles (4) makes algebraic solutions to (7) and hence to (10) tedious, if even possible. This makes it difficult gain insight into the role of edge effects in restricting the FOV. Instead, we pursue such intuition by examining closed-form solutions to (10) for the special, restricted case $\phi = \pi/2$ (2). First note that (10) is equivalent to

$$\begin{aligned}
\bar{\psi}(z; R_s, R) &\equiv \frac{1}{\pi R^2} \int_0^R 2\pi r \bar{\psi}(r, z; R_s) dr \\
&= \frac{2}{R^2} \int_0^R r [\pi - (\bar{\psi}_1 + \bar{\psi}_2)] dr \\
&= \pi - \frac{2}{R^2} \int_0^R r [\bar{\psi}_1(r, z; R_s) + \bar{\psi}_2(r, z; R_s)] dr
\end{aligned} \tag{11}$$

To proceed further, replace $\bar{\psi}_1(r, z; R_s)$ and $\bar{\psi}_2(r, z; R_s)$ in (11) with $\psi_1(r, \phi = \pi/2, z; R_s)$ and $\psi_2(r, \phi = \pi/2, z; R_s)$ (2), respectively, to obtain:

$$\begin{aligned}
\bar{\psi}(\phi = \pi/2, z; R_s, R) &= \pi - \frac{2}{R^2} \int_0^R r [\psi_1(r, \phi = \pi/2, z; R_s) + \psi_2(r, \phi = \pi/2, z; R_s)] dr \\
&= \pi - \frac{2}{R^2} \int_0^R r \left[\arctan \left(\frac{z}{R_s - r} \right) + \arctan \left(\frac{z}{R_s + r} \right) \right] dr
\end{aligned} \tag{12}$$

The elimination of the azimuthal integral makes (12) considerably simpler than (10). The algebraic solution to (12) involves integration-by-parts, and is, as verified by Mathematica ([Wolfram Research, 2008](#)):

$$\begin{aligned}
\int x \arctan \left(\frac{a}{b \pm x} \right) dx &= \frac{x^2}{2} \arctan \left(\frac{a}{b \pm x} \right) \pm \frac{ax}{2} \mp \frac{(a^2 - b^2)}{2} \arctan \left(\frac{x \pm b}{a} \right) \\
&\quad - \frac{ab}{2} \ln(a^2 + b^2 + x^2 \pm 2bx) + C
\end{aligned} \tag{13}$$

so that the indefinite integral required to evaluate (12) reduces to

$$\begin{aligned}
&\int x \arctan \left(\frac{a}{b+x} \right) + x \arctan \left(\frac{a}{b-x} \right) dx = \\
&\frac{x^2}{2} \left[\arctan \left(\frac{a}{b+x} \right) + \arctan \left(\frac{a}{b-x} \right) \right] + \frac{b^2 - a^2}{2} \left[\arctan \left(\frac{x+b}{a} \right) - \arctan \left(\frac{x-b}{a} \right) \right] \\
&\quad - \frac{ab}{2} \ln[(a^2 + b^2 + x^2 + 2bx)(a^2 + b^2 + x^2 - 2bx)] + C
\end{aligned} \tag{14}$$

223 where $a = z$, $b = R_s$, and $x = r$. Examination of (14) shows how snow depth z and distance from
 224 sample axis r contribute individually and in-tandem to the angle available for up-scattered photons
 225 to enter the integrating sphere.

226 The crude, two-dimensional simplification (12) lacks the full three-dimensional physics em-
 227 bodied in the general form (10). We used (12) to investigate aperture characteristics and to verify
 228 limiting cases of the general solution (10). Regardless of whether any approximation is used to
 229 compute $\bar{\psi}$, one must eventually convert from planar to solid angles to obtain the field-of-view
 230 (FOV).

Rotating the aperture-mean mean-planar angle $\bar{\psi}$ (10) about the vertical axis z does not yield
 the aperture-mean solid angle FOV (because “the average of the cosine is not the cosine of the
 average”). The half-angle formula expresses $\cos(\psi/2)$ in terms of $\cos \psi$,

$$\cos \frac{\psi}{2} = \pm \sqrt{\frac{1 + \cos \psi}{2}} \quad (15)$$

Applying the half-angle formula (15) to the solid angle of rotation (8),

$$\Omega(r, z; R_s) = 2\pi \left(1 - \sqrt{\frac{1 + \cos \bar{\psi}(r, z; R_s)}{2}} \right) \quad (16)$$

231 Given that ψ is a function (1) of angles whose tangents are known (4), it is possible, for restricted
 232 values of ϕ , to solve (16) algebraically.

The mean FOV approximation (9) applies a snow sample of uniformly illuminated size R . The
 diode laser emits into the snow sample a collimated beam of width $R_b < R_s$. Snow experiencing
 this “direct” illumination (i.e., by photons not yet scattered by the sphere walls) is more “on-center”
 and has a greater FOV than diffusely illuminated snow. We assume that diffuse illumination, i.e.,
 radiation previously scattered by the spherical walls, uniformly illuminates the sample across the
 entire aperture. Hence the mean FOV’s of the directly and diffusely illuminated snow, $\bar{\Omega}^\circ(z)$ and
 $\bar{\Omega}^d(z)$, respectively, are obtained by setting $R = R_b$ and $R = R_s$ in (10), (12), and (9):

$$\bar{\Omega}^\circ(z) = \bar{\Omega}(z; R_s, R = R_b) \quad (17a)$$

$$\bar{\Omega}^d(z) = \bar{\Omega}(z; R_s, R = R_s) \quad (17b)$$

233 Beam widths are $R_b = 0.5, 0.5, 0.5$ cm for wavelengths $\lambda = 635, 1310, 1550$ nm, respectively.

234 Table ?? shows the mean FOV’s (17) as a function of depth z within the sample holder. In
 235 terms of fractional hemispheres (multiply by 2π to convert to steradians) so that surface snow has
 236 $\bar{\Omega}(0) = 1$.

237 6.2 Direct vs. Diffuse partitioning

238 To account for the directional properties of snow reflectance (*Warren and Wiscombe, 1980*) one
 239 must know the direct/diffuse partitioning of the incident radiation. The diode laser emits colli-
 240 mated radiation directly down into the snow sample where some is (eventually) absorbed and from
 241 which the rest is up-scattered. The integrating sphere converts up-scattered radiation into (approx-
 242 imately) isotropic radiation that (usually) interacts multiple times with the sample along with the

243 direct beam. Thus the snow sample simultaneously receives both collimated (direct) and diffuse
 244 radiation. The question to answer is: what fraction of each?

245 Integrating sphere experiments may be modeled as Markov processes in that the relative surface
 246 areas and reflectivities of the various sphere components deterministically predict the evolution
 247 of photon states from emission through absorption. *Hidović-Rowe et al. (2006)* and references
 248 therein describe and evaluate the assumptions underlying this claim. We adopt their Markov-
 249 process formalism to estimate the direct/diffuse partitioning of radiation incident on the sample.
 250 This requires specifying the matrix of transition probabilities of photon states within the integrating
 251 sphere. The following discussion utilizes the nomenclature and symbols of *Hidović-Rowe et al.*
 252 (2006).

The transition matrix that describes photon states within the sphere depends on geometry and
 absorption/reflection characteristics. We consider an integrating sphere comprising a sample, de-
 tector, and “holes” (namely the diode-laser aperture) of sizes s , d , and h , respectively. All sizes
 are surface areas normalized and non-dimensionalized by $4\pi R_{\text{IS}}^2$ so that the total integrating sphere
 chamber has unity size. In this system, the normalized area α of reflective spherical walls is

$$\alpha = 1 - s - d - h \quad (18)$$

253 After their first reflection, photons emitted into the sphere are assumed to be in one of $n = 6$
 254 possible states comprising $m = 4$ absorbing states and $l \equiv n - m = 2$ reflecting states. Photon
 255 states are named by the interaction type (absorbing or reflecting) and the element of the integrating
 256 sphere apparatus with which the interaction occurred. There are four elements in the apparatus,
 257 all of which may absorb photons: 1. Detector, 2. Sample (i.e., snow), 3. Holes (i.e., diode-laser),
 258 4. Walls. Thus absorbed photons may be in states AD, AS, AH, and AW, respectively. After
 259 absorption, photons cease activity (no further transitions allowed).

260 We assume that only the walls and the sample may reflect photons. Photons may be in one of
 261 two reflecting states, reflected (most recently) by the wall (RW) or by the sample (RS). No other
 262 states are allowed.

The transition matrix P among the six states is

$$P_{i,j} = \begin{array}{c|cccccc} & \text{AD} & \text{AS} & \text{AH} & \text{AW} & \text{RS} & \text{RW} \\ \hline \text{AD} & 1 & 0 & 0 & 0 & 0 & 0 \\ \text{AS} & 0 & 1 & 0 & 0 & 0 & 0 \\ \text{AH} & 0 & 0 & 1 & 0 & 0 & 0 \\ \text{AW} & 0 & 0 & 0 & 1 & 0 & 0 \\ \text{RS} & d & (1-r)s & h & (1-w)\alpha & rs & w\alpha \\ \text{RW} & d & (1-r)s & h & (1-w)\alpha & rs & w\alpha \end{array} \quad (19)$$

263 where i denotes the row (current photon state) and j denote the column (next state). For example,
 264 the probability that a photon most recently reflected by the walls will next reflect off the sample is
 265 $P(\text{RW} \rightarrow \text{RS}) = P_{6,5} = rs$. Note that the sum of each row is (and must be) one.

By construction the transition matrix comprises four sub-matrices

$$P = \begin{pmatrix} I & 0 \\ R & T \end{pmatrix} \quad (20)$$

266 where the $m \times m$ diagonal identity matrix I defines the transition probabilities among absorbing
 267 states, the $m \times l$ zero matrix 0 contains the transition probabilities from absorbing to reflecting

268 states, the $l \times m$ matrix R characterizes transitions from reflecting to absorbing states, and the $l \times l$
 269 matrix T characterizes transitions from reflecting to reflecting states.

The fundamental matrix Q of the system is

$$Q = (I - T)^{-1} \quad (21)$$

270 As summarized in *Hidović-Rowe et al. (2006)*, Q defines the number of times each state is visited.
 271 Therefore the product QR defines the probability of ending in each absorbing state, starting from
 272 any initial state. The product QT gives the likelihood that, starting from a given reflecting state, a
 273 photon will next enter another reflecting state.

The integrating sphere described by (19) represents the simplest apparatus considered here and in *Hidović-Rowe et al. (2006)* and has optical property matrices

$$R = \begin{pmatrix} d & (1-r)s & h & (1-w)\alpha \\ d & (1-r)s & h & (1-w)\alpha \end{pmatrix} \quad (22)$$

$$T = \begin{pmatrix} rs & w\alpha \\ rs & w\alpha \end{pmatrix} \quad (23)$$

$$Q = \beta_1 \begin{pmatrix} 1 - w\alpha & w\alpha \\ rs & 1 - rs \end{pmatrix} \quad \text{where} \quad (24a)$$

$$\beta_1 \equiv (1 - rs - w\alpha)^{-1} \quad (24b)$$

and

$$QR = \beta_1 \begin{pmatrix} d & s(1-r) & h & \alpha(1-w) \\ d & s(1-r) & h & \alpha(1-w) \end{pmatrix} \quad (25)$$

$$QT = \beta_1 \begin{pmatrix} rs & w\alpha \\ rs & w\alpha \end{pmatrix} \quad (26)$$

The long-term statistics of the system (25)–(26) describe the quantity of immediate interest, i.e., the relative fractions of incident direct and diffuse radiation. Because the diode laser in our integrating sphere emits a collimated beam directly onto the snow sample, diffuse radiation must initially reflect from the sample surface and then from a wall. The fraction of emitted photons that initially backscatter from the sample surface is the direct albedo \dot{r} , not to be confused with the albedo to diffuse radiation r . We idealize the snow as a Lambertian surface so that backscattered radiation is isotropic. Hence, the fraction f_{RS}^\dagger of emitted photons that start in state RS and are then subject to the transition matrix rules (19)–(26) is

$$f_{RS}^\dagger = \dot{r} \quad (27)$$

The transformation of this state RS radiation (27) into diffuse radiation incident on the snow-pack is described by a combination of three long-term probabilities. First, the state RS photons must reflect from walls to become state RW photons. This probability is

$$P(RS \rightarrow RW) = P_{5,6} = w\alpha \quad (28)$$

The fraction f_{RW}^\uparrow of emitted photons that progress to state RW is therefore (27) times (28)

$$\begin{aligned} f_{\text{RW}}^\uparrow &= f_{\text{RS}}^\uparrow \times P(\text{RS} \rightarrow \text{RW}) \\ &= \dot{r}w\alpha \end{aligned} \quad (29)$$

The likelihood that diffuse radiation strikes the snow sample (i.e., after reflecting from a wall) is the union (sum) of the probabilities that state RW photons transition to state RS or AS photons in the long term, i.e.,

$$\begin{aligned} p(\text{RW} \rightarrow \text{RS}|\text{AS}) &= QT(\text{RW} \rightarrow \text{RS}) + QR(\text{RW} \rightarrow \text{AS}) \\ &= (QT)_{2,1} + (QR)_{2,2} \\ &= rs\beta_1 + s(1-r)\beta_1 \\ &= \beta_1 s \\ &= s/(1-rs-w\alpha) \end{aligned} \quad (30)$$

The diffuse radiation incident on the sample comprises the initial fraction of backscattered photons that then reflect off a wall and, eventually, back to the sample. These events are independent so the probability of their all occurring is the product of their individual probabilities. Hence the diffuse radiation f_{d}^\downarrow incident on the sample is, as a fraction of the laser-emitted radiation, the product of (27)–(30):

$$\begin{aligned} f_{\text{d}}^\downarrow &= f_{\text{RW}}^\uparrow \times p(\text{RW} \rightarrow \text{RS}|\text{AS}) \\ &= f_{\text{RS}}^\uparrow \times P(\text{RS} \rightarrow \text{RW}) \times p(\text{RW} \rightarrow \text{RS}|\text{AS}) \\ &= \dot{r} \times w\alpha \times s/(1-rs-w\alpha) \\ &= \frac{\dot{r}w\alpha s}{1-rs-w\alpha} \end{aligned} \quad (31)$$

In practice some of the laser-emitted radiation diverges from the collimated beam and strikes the reflective sphere before the snow sample. Imperfections in the laser optics cause this “stray light”. We assume that a fraction \tilde{f} of laser-emitted photons enter the sphere as diffuse illumination. The conservative assumption is that those diffuse-emitted photons that reflect from the first wall immediately enter state RW. This “RW-assumption” for the mixture of stray and collimated light emitted by the laser, in fractions \tilde{f} and \dot{f} , respectively, supercedes (29), which assumed entirely collimated light incident on the sample, and leads instead to

$$\begin{aligned} f_{\text{RW}}^\uparrow &= \dot{f}\dot{r}w\alpha + \tilde{f}w \\ &= \dot{f}\dot{r}w\alpha + (1-\dot{f})w \\ &= [1 + \dot{f}(\dot{r}\alpha - 1)]w \end{aligned} \quad (32)$$

where conservation of the emitted photons is expressed by

$$\tilde{f} + \dot{f} \equiv 1 \quad (33)$$

The diffuse-emitted photons are indistinct from the direct-emitted (collimated) photons except that the former first strike the sphere walls and the latter first strike the sample surface. Laser-design ensures, and observations confirm, that the emitted photon flux peaks at, and diminishes

radially outwards from, the sample center. With this picture in mind, we see that the majority of diffuse-emitted photons probably act like state RS photons after the first reflection, and require a second reflection before behaving like isotropic state RW photons. Under this “RS-assumption” the correction of (29) becomes

$$\begin{aligned}
f_{\text{RW}}^{\uparrow} &= \dot{f} \dot{r} w \alpha + \tilde{f} w^2 \alpha \\
&= \dot{f} \dot{r} w \alpha + (1 - \dot{f}) w^2 \alpha \\
&= [w + \dot{f}(\dot{r} - w)] w \alpha
\end{aligned} \tag{34}$$

274 Laser diode optics are usually good enough to assume that $\tilde{f} \ll \dot{f}$. However, it may simul-
275 taneously be true that $\dot{r} \ll w$ at near-infrared wavelengths and/or for heavily contaminated snow
276 samples. In such cases stray light makes a considerable contribution to f_{RW}^{\uparrow} (32). This contribution
277 causes the detector to measure a signal even for perfectly black samples. It is important to estimate
278 the size of the expected signal from stray light, especially for low reflectance surfaces.

The detected light is determined by the long term transition probability that the reflected light enters state AD, i.e., is absorbed by the detector. If all light is collimated and strikes the sample first, then this probability is $QR(\text{RS} \rightarrow \text{AD})$ and the measured signal m is

$$\begin{aligned}
m &= f_{\text{RS}}^{\uparrow} \times QR(\text{RS} \rightarrow \text{AD}) \\
&= f_{\text{RS}}^{\uparrow} \times (QR)_{1,1} \\
&= \dot{r} \times d\beta_1 \\
&= \dot{r} d\beta_1 \\
&= \frac{\dot{r} d}{1 - rs - w\alpha}
\end{aligned} \tag{35}$$

279 The measured signal is proportional to the direct reflectance and to the detector area.

If we account for the presence of stray-emitted photons and make the “RW-assumption” (32) then

$$\begin{aligned}
m &= \dot{f} \times f_{\text{RS}}^{\uparrow} \times QR(\text{RS} \rightarrow \text{AD}) + \tilde{f} \times f_{\text{RW}}^{\uparrow} \times QR(\text{RW} \rightarrow \text{AD}) \\
&= \dot{f} \times f_{\text{RS}}^{\uparrow} \times (QR)_{1,1} + (1 - \dot{f}) \times f_{\text{RW}}^{\uparrow} \times (QR)_{2,1} \\
&= \dot{f} \dot{r} d\beta_1 + (1 - \dot{f}) w d\beta_1 \\
&= [\dot{f} \dot{r} + (1 - \dot{f}) w] d\beta_1 \\
&= \frac{[\dot{f} \dot{r} + (1 - \dot{f}) w] d}{1 - rs - w\alpha}
\end{aligned} \tag{36}$$

280 The stray light contributes a signal independent of \dot{r} , in contrast to (35).

When we account for the presence of stray-emitted photons and make the “RW-assumption”

(32) the measured signal in integrating sphere with a flat sample and an optical baffle becomes

$$\begin{aligned}
m &= \dot{f} \times f_{\text{RS}}^\uparrow \times QR(\text{RS} \rightarrow \text{AD}) + \tilde{f} \times f_{\text{RW}}^\uparrow \times QR(\text{RW} \rightarrow \text{AD}) \\
&= \dot{f} \times f_{\text{RS}}^\uparrow \times (QR)_{1,1} + (1 - \dot{f}) \times f_{\text{RW}}^\uparrow \times (QR)_{2,1} \\
&= \dot{f} \times r \times \frac{dw\alpha\beta_3}{1 - (s + d)} + (1 - \dot{f}) \times w \times d\beta_3 \\
&= \frac{\dot{f}rdw\alpha\beta_3}{1 - (s + d)} + (1 - \dot{f})wd\beta_3 \\
&= \left(\frac{\dot{f}r\alpha}{1 - (s + d)} + (1 - \dot{f}) \right) \times wd\beta_3 \\
&= \left(\frac{\dot{f}r\alpha}{1 - (s + d)} + (1 - \dot{f}) \right) \times \frac{1 - (s + d)}{1 - (s + d) - w\alpha\{1 - [d + (1 - r)s]\}} \times wd \\
&= \frac{wd\{\dot{f}r\alpha + (1 - \dot{f})[1 - (s + d)]\}}{1 - (s + d) - w\alpha\{1 - [d + (1 - r)s]\}} \tag{37}
\end{aligned}$$

The contribution of (initially) diffuse illumination to illumination of the sample follows the logic leading to (31), with the exception that the photons in state RW are assumed to follow either the ‘‘RW-assumption’’ (32) or the ‘‘RS-assumption’’ (34). Correcting the estimate of diffuse downwelling radiation f_d^\downarrow (31) to account for emission fractions \dot{f} and \tilde{f} initially striking the sample and the sphere walls, respectively, under the ‘‘RW-assumption’’, yields

$$\begin{aligned}
f_d^\downarrow &= f_{\text{RW}}^\uparrow \times p(\text{RW} \rightarrow \text{RS}||\text{AS}) \\
&= [1 + \dot{f}(r\alpha - 1)]w \times s / (1 - rs - w\alpha) \\
&= \frac{[1 + \dot{f}(r\alpha - 1)]ws}{1 - rs - w\alpha} \tag{38}
\end{aligned}$$

Two geometric refinements to the simple integrating sphere described above improve the representation of the actual integrating sphere. Both refinements were suggested by *Hidović-Rowe et al.* (2006). The first correction makes the sample flat rather than curved. A flat sample has

$$P(\text{RS} \rightarrow \text{AS}) = P_{5,2} = P(\text{RS} \rightarrow \text{RS}) = P_{5,5} = 0 \tag{39}$$

Photons reflected by a flat sample cannot next be absorbed or reflected by the sample. Therefore the photon interaction probability with all other surfaces must increase by a factor $(1 - s)^{-1}$. Transitions from the RS state occur with larger probabilities than predicted solely by the geometric area of the next state. Re-normalizing the RS row in (19) by $(1 - s)$, we obtain the transition matrix P' for the integrating sphere with the flat sample

	AD	AS	AH	AW	RS	RW
AD	1	0	0	0	0	0
AS	0	1	0	0	0	0
AH	0	0	1	0	0	0
AW	0	0	0	1	0	0
RS	$d/(1 - s)$	0	$h/(1 - s)$	$(1 - w)\alpha/(1 - s)$	0	$w\alpha/(1 - s)$
RW	d	$(1 - r)s$	h	$(1 - w)\alpha$	rs	$w\alpha$

(40)

The same procedures applied to P (19) to obtain (22)–(26) must be applied to P' (40) to obtain the fundamental matrix and long-term transition probabilities of the integrating sphere with a flat sample. For simplicity we omit the prime notation.

$$R = \begin{pmatrix} \frac{d}{1-s} & 0 & \frac{h}{1-s} & \frac{(1-w)\alpha}{1-s} \\ d & (1-r)s & h & (1-w)\alpha \end{pmatrix} \quad (41)$$

$$T = \begin{pmatrix} 0 & \frac{w\alpha}{1-s} \\ rs & w\alpha \end{pmatrix} \quad (42)$$

$$Q = \beta_2 \begin{pmatrix} 1-w\alpha & \frac{w\alpha}{1-s} \\ rs & 1 \end{pmatrix} \quad \text{where} \quad (43a)$$

$$\beta_2 \equiv \frac{1-s}{1-s-w\alpha[1-(1-r)s]} \quad (43b)$$

and

$$QR = \beta_2 \begin{pmatrix} \frac{d}{1-s} & \frac{sw\alpha}{(1-r)(1-s)} & \frac{h}{1-s} & \frac{(1-w)\alpha}{1-s} \\ \frac{d[1-(1-r)s]}{1-s} & (1-r)s & \frac{h[1-(1-r)s]}{1-s} & \frac{(1-w)\alpha[1-(1-r)s]}{1-s} \end{pmatrix} \quad (44)$$

$$QT = \beta_2 \begin{pmatrix} \frac{rsw\alpha}{1-s} & \frac{w\alpha}{1-s} \\ rs & \frac{w\alpha[1-(1-r)s]}{1-s} \end{pmatrix} \quad (45)$$

Correcting the estimate of diffuse downwelling radiation f_d^\downarrow (31) to account for the refined (flat sample) geometry leads to

$$\begin{aligned} f_d^\downarrow &= f_{RS}^\uparrow \times P(RS \rightarrow RW) \times p(RW \rightarrow RS||AS) \\ &= \dot{r} \times P(RS \rightarrow RW) \times p(RW \rightarrow RS||AS) \\ &= \dot{r} \times w\alpha/(1-s) \times \beta_2 s \\ &= \frac{\dot{r}w\alpha s}{1-s-w\alpha[1-s(1-r)]} \end{aligned} \quad (46)$$

The second refinement made to the simple sphere (19) simulates the optical baffle between the sample and the detector. This small baffle (radius = fxm) prevents any specular reflection of the incident collimated laser beam from reaching the detector so

$$P(RS \rightarrow AD) = P_{5,1} = 0 \quad (47)$$

This alone increases the interaction probability of state RS photons with the permitted transitions of (19) by a factor $(1-d)^{-1}$. The baffle and flat-sample conditions together increase the interaction probability of state RS photons with the remaining permitted transitions (to AH, AW, and RW) of

(19) by a combined factor $[1 - (s + d)]^{-1}$. This factor is simply the inverse relative surface area of the permitted transitions. Re-normalizing the RS row in (19) by $[1 - (s + d)]^{-1}$, we obtain the transition matrix P'' for the integrating sphere with the flat sample and an optical baffle to specular reflection

$$P''_{i,j} = \begin{array}{c|cccccc} & \text{AD} & \text{AS} & \text{AH} & \text{AW} & \text{RS} & \text{RW} \\ \hline \text{AD} & 1 & 0 & 0 & 0 & 0 & 0 \\ \text{AS} & 0 & 1 & 0 & 0 & 0 & 0 \\ \text{AH} & 0 & 0 & 1 & 0 & 0 & 0 \\ \text{AW} & 0 & 0 & 0 & 1 & 0 & 0 \\ \text{RS} & 0 & 0 & h/[1 - (s + d)] & (1 - w)\alpha/[1 - (s + d)] & 0 & w\alpha/[1 - (s + d)] \\ \text{RW} & d & (1 - r)s & h & (1 - w)\alpha & rs & w\alpha \end{array} \quad (48)$$

The same procedures applied to P (19) to obtain (22)–(26) must be applied to P'' (48) to obtain the fundamental matrix and long-term transition probabilities of the integrating sphere with a flat sample and an optical baffle to specular reflection. For simplicity we omit the prime notation.

$$R = \begin{pmatrix} 0 & 0 & \frac{h}{1 - (s + d)} & \frac{(1 - w)\alpha}{1 - (s + d)} \\ d & (1 - r)s & h & (1 - w)\alpha \end{pmatrix} \quad (49)$$

$$T = \begin{pmatrix} 0 & \frac{w\alpha}{1 - (s + d)} \\ rs & w\alpha \end{pmatrix} \quad (50)$$

$$Q = \beta_3 \begin{pmatrix} 1 - w\alpha & \frac{w\alpha}{1 - (s + d)} \\ rs & 1 \end{pmatrix} \quad \text{where} \quad (51a)$$

$$\beta_3 \equiv \frac{1 - (s + d)}{1 - (s + d) - w\alpha\{1 - [d + (1 - r)s]\}} \quad (51b)$$

and

$$QR = \beta_3 \begin{pmatrix} \frac{dw\alpha}{1 - (s + d)} & \frac{(1 - r)sw\alpha}{1 - (s + d)} & \frac{h}{1 - (s + d)} & \frac{1 - w\alpha}{1 - (s + d)} \\ d & (1 - r)s & \frac{h\{1 - [d + (1 - r)s]\}}{1 - (s + d)} & \frac{(1 - w)\alpha\{1 - [d + (1 - r)s]\}}{1 - (s + d)} \end{pmatrix} \quad (52)$$

$$QT = \beta_3 \begin{pmatrix} \frac{rsw\alpha}{1 - (s + d)} & \frac{w\alpha}{1 - (s + d)} \\ rs & \frac{w\alpha\{1 - [d + (1 - r)s]\}}{1 - (s + d)} \end{pmatrix} \quad (53)$$

Correcting the estimate of diffuse downwelling radiation f_d^\dagger (31) to account for the refined (flat

sample with baffle to specular reflection) geometry leads to

$$\begin{aligned}
f_d^\downarrow &= f_{RS}^\uparrow \times P(RS \rightarrow RW) \times p(RW \rightarrow RS||AS) \\
&= \dot{r} \times P(RS \rightarrow RW) \times p(RW \rightarrow RS||AS) \\
&= \dot{r} \times w\alpha/[1 - (s + d)] \times \beta_3 s \\
&= \frac{\dot{r}w\alpha s}{1 - (s + d) - w\alpha\{1 - [d + (1 - r)s]\}}
\end{aligned} \tag{54}$$

Correcting the preceding expression (54) to account for emission fractions \dot{f} and \tilde{f} initially striking the sample and the sphere walls, respectively, under the ‘‘RW-assumption’’, yields

$$\begin{aligned}
f_d^\downarrow &= [f_{RS}^\uparrow \times P(RS \rightarrow RW) + f_{RW}^\uparrow] \times p(RW \rightarrow RS||AS) \\
&= \left[\dot{f}\dot{r} \times \frac{w\alpha}{1 - (s + d)} + (1 - \dot{f})w \right] \times \beta_3 s \\
&= \left[\dot{f}\dot{r} \times \frac{w\alpha}{1 - (s + d)} + (1 - \dot{f})w \right] \times \frac{s[1 - (s + d)]}{1 - (s + d) - w\alpha\{1 - [d + (1 - r)s]\}} \\
&= \frac{ws\{\dot{f}\dot{r}\alpha + [1 - (s + d)](1 - \dot{f})\}}{1 - (s + d) - w\alpha\{1 - [d + (1 - r)s]\}}
\end{aligned} \tag{55}$$

281 6.3 Sample Penetration

282 As mentioned above, deeper snow contributes less to surface reflectance for two independent rea-
283 sons: screening by upper layers and smaller fields-of-view (FOV) into the integrating sphere.

The reduced albedo contribution by deeper sample layers is estimated the layer contribution to surface albedo weighted by the layer solid-angle correction (17). The layer contribution to surface albedo is estimated using the adding method for homogeneous layers in the delta-Eddington approximation (Joseph et al., 1976). The delta-Eddington approximation solves the two-stream radiative transfer equations for the scaled optical properties defined by

$$\tau_e^* = \tau_e(1 - \varpi f) \tag{56}$$

$$\varpi^* = \varpi \left(\frac{1 - f}{1 - \varpi f} \right) \tag{57}$$

$$g^* = \frac{g - f}{1 - f} \tag{58}$$

284 where τ_e is the extinction optical depth, ϖ is the single scattering albedo, g is the asymmetry pa-
285 rameter, and f is the radiation fraction assumed scattered into the delta-function forward peak and
286 is assumed to equal the second moment of the phase function expansion into Legendre polynomials
287 (Joseph et al., 1976).

The solution to the delta-Eddington approximation can be written as a collection of layer re-
reflectances and transmissions to direct and diffuse incident radiation (Wiscombe, 1977). These re-
reflectances and transmissions depend on a number of intermediate parameters that, for convenience,

we show in order of their computational dependence. Following the nomenclature of *Coakley et al. (1983)*, the intermediate parameters that depend on the scaled optical properties (57)–(58) as

$$\lambda = \sqrt{3(1 - \varpi^*)(1 - \varpi^*g^*)} \quad (59)$$

$$\alpha = \frac{3\varpi^*\mu_0}{4} \left(\frac{1 + g^*(1 - \varpi^*)}{1 - \lambda^2\mu_0^2} \right) \quad (60)$$

$$\gamma = \frac{\varpi^*}{2} \left(\frac{1 + 3g^*(1 - \varpi^*)\mu_0^2}{1 - \lambda^2\mu_0^2} \right) \quad (61)$$

$$u = \frac{3}{2}(1 - \varpi^*g^*\lambda) \quad (62)$$

$$N = (u + 1)^2 e^{\lambda\tau_e^*} - (u - 1)^2 e^{-\lambda\tau_e^*} \quad (63)$$

288 where μ_0 is the cosine of the solar zenith angle.

The layer reflectances and transmissions in the delta-Eddington approximation follow from the parameters (59)–(63). First, the reflectance \bar{R} and transmittance \bar{T} of a homogeneous layer to isotropic incident radiation are

$$\bar{R} = (u + 1)(u - 1)(e^{\lambda\tau_e^*} - e^{-\lambda\tau_e^*})/N \quad (64)$$

$$\bar{T} = 4u/N \quad (65)$$

Next, it is helpful to distinguish between the two most common types of transmittance for they are easily confused. The *direct-beam transmittance* \dot{T}^\odot is the ratio of the direct beam exiting a layer to the direct beam incident on the layer.

$$\dot{T}^\odot = e^{-\tau_e^*/\mu_0} \quad (66)$$

289 The direct-beam transmittance simply expresses Beer's law. We will see that \dot{T}^\odot (66) attenuates
290 many factors that occur in the direct reflectances and total transmittances (67)–(68).

The second common form of transmittance is the *total transmittance* \dot{T} to direct-incident radiation. This is the sum of direct *and* diffuse flux exiting the layer divided by the direct flux entering the layer. With this distinction in mind, we can finally define the the reflectance \dot{R} and the total transmittance \dot{T} of a homogeneous layer to direct-incident radiation ¹

$$\begin{aligned} \dot{R} &= (\alpha - \gamma)\bar{T}e^{-\tau_e^*/\mu_0} + (\alpha + \gamma)\bar{R} - (\alpha - \gamma) \\ &= (\alpha - \gamma)\bar{T}\dot{T}^\odot + (\alpha + \gamma)\bar{R} - (\alpha - \gamma) \end{aligned} \quad (67)$$

$$\begin{aligned} \dot{T} &= (\alpha + \gamma)\bar{T} + (\alpha - \gamma)\bar{R}e^{-\tau_e^*/\mu_0} - (\alpha + \gamma - 1)e^{-\tau_e^*/\mu_0} \\ &= (\alpha + \gamma)\bar{T} + [(\alpha - \gamma)\bar{R} - (\alpha + \gamma - 1)]\dot{T}^\odot \end{aligned} \quad (68)$$

291 As mentioned earlier, both \dot{R} (67) and \dot{T} (68) depend on \dot{T}^\odot (66).

292 Procedures to determine the reflectances and transmittances of inhomogeneous layers include
293 the discrete ordinates (*Stamnes et al., 1988*) and adding-doubling (*Hunt, 1971*) methods. These
294 methods decompose the inhomogeneous layer into a stack of homogeneous layers. Such decom-
295 positions involve scale-dependent assumptions that we will ignore.

¹Note that the multiplier of the \bar{R} term in (67) is $(\alpha + \gamma)$ not $(\alpha - \gamma)$. This correction, also present in *Collins et al. (2006)*, fixes a typo in *Coakley et al. (1983)* Equation (B1).

296 The relative contribution of depth z snow to the total sample albedo is of primary interest. This
 297 contribution reveals whether the sample holder is deep enough to appear semi-infinite. The two-
 298 stream approximation with delta-Eddington correction (*Joseph et al., 1976*) is sufficiently accurate
 299 for our purposes of determining relative albedo contributions (*Warren and Wiscombe, 1980*).

300 The adding procedure for combining optical properties of homogeneous layers is exact and
 301 may be applied to any number of radiances or “streams” or radiation. We derive the procedure for
 302 S -streams, and then apply it for $S = 2$ following *Coakley et al. (1983)*. The system comprises
 303 N homogeneous layers surrounded by $N + 1$ interfaces. Layer 1 is, by convention, beneath inter-
 304 face 0 and above interface 1. An arbitrary layer k is beneath interface $k - 1$ and is above interface k .
 305 The S -element vectors \mathbf{I}_k^+ and \mathbf{I}_k^- contain the up- and down-welling radiances, respectively, that
 306 cross interface level k .

Each layer reflects and transmits the incident radiances from above and below. The $S \times S$ -
 element reflection and transmission matrices for each layer, R_k and T_k , respectively, transform the
 incident radiances into exitant radiances. The incident and exitant intensities are, at level zero (top
 of layer 1),

$$\mathbf{I}_0^+ = R_1 \mathbf{I}_0^- + T_1 \mathbf{I}_1^+ \quad (69a)$$

$$\mathbf{I}_0^- = \text{Boundary Condition} \quad (69b)$$

and are, at level one (bottom of layer 1 and top of layer 2),

$$\mathbf{I}_1^+ = R_2 \mathbf{I}_1^- + T_2 \mathbf{I}_2^+ \quad (70a)$$

$$\mathbf{I}_1^- = R_1 \mathbf{I}_2^+ + T_1 \mathbf{I}_0^- \quad (70b)$$

and are, at general level k (bottom of layer k and top of layer $k + 1$),

$$\mathbf{I}_k^+ = R_{k+1} \mathbf{I}_k^- + T_{k+1} \mathbf{I}_{k+1}^+ \quad (71a)$$

$$\mathbf{I}_k^- = R_k \mathbf{I}_{k+1}^+ + T_k \mathbf{I}_{k-1}^- \quad (71b)$$

What we seek from this set of coupled matrix equations is a method to obtain the equivalent
 optical properties of an arbitrary number of layers. First we eliminate \mathbf{I}_1^- from the expression for
 \mathbf{I}_1^+ by inserting (70b) into (70a),

$$\begin{aligned} \mathbf{I}_1^+ &= R_2(R_1 \mathbf{I}_1^+ + T_1 \mathbf{I}_0^-) + T_2 \mathbf{I}_2^+ \\ \mathbf{I}_1^+ &= R_2 R_1 \mathbf{I}_1^+ + R_2 T_1 \mathbf{I}_0^- + T_2 \mathbf{I}_2^+ \\ (1 - R_2 R_1) \mathbf{I}_1^+ &= R_2 T_1 \mathbf{I}_0^- + T_2 \mathbf{I}_2^+ \\ (1 - R_2 R_1)^{-1} (1 - R_2 R_1) \mathbf{I}_1^+ &= (1 - R_2 R_1)^{-1} R_2 T_1 \mathbf{I}_0^- + (1 - R_2 R_1)^{-1} T_2 \mathbf{I}_2^+ \\ \mathbf{I}_1^+ &= (1 - R_2 R_1)^{-1} R_2 T_1 \mathbf{I}_0^- + (1 - R_2 R_1)^{-1} T_2 \mathbf{I}_2^+ \end{aligned} \quad (72)$$

307 where $\mathbf{1} \equiv I$ is the (diagonal) identity matrix $I_{i,j} = \delta(i - j)$ and the negative one exponent applied
 308 to matrices (e.g., R^{-1}) refers to matrix inversion. Note that the matrix algebra just applied is *not*
 309 commutative over multiplication.

We eliminate \mathbf{I}_1^+ from the expression for \mathbf{I}_0^+ by inserting (72) into (69a),

$$\begin{aligned} \mathbf{I}_0^+ &= R_1 \mathbf{I}_0^- + T_1 [(1 - R_2 R_1)^{-1} R_2 T_1 \mathbf{I}_0^- + (1 - R_2 R_1)^{-1} T_2 \mathbf{I}_2^+] \\ &= [R_1 + T_1 (1 - R_2 R_1)^{-1} R_2 T_1] \mathbf{I}_0^- + T_1 (1 - R_2 R_1)^{-1} T_2 \mathbf{I}_2^+ \end{aligned} \quad (73)$$

Examination of (73) shows that the (matrix) coefficients of \mathbf{I}_0^- and \mathbf{I}_2^+ express the reflectance and transmittance, respectively, of the (inhomogeneous) two-layer system. More specifically, we define

$$R_{21} \equiv R_1 + T_1(1 - R_2R_1)^{-1}R_2T_1 \quad (74a)$$

$$T_{12} \equiv T_1(1 - R_2R_1)^{-1}T_2 \quad (74b)$$

so that (73) may also be written as

$$\mathbf{I}_0^+ = R_{21}\mathbf{I}_0^- + T_{12}\mathbf{I}_2^+ \quad (75)$$

310 Note carefully the subscript ordering² R_{21} in (74a) is the reflectance matrix that transforms down-
 311 welling radiation incident on the two-layer system (recall that layer 1 is above layer 2) from above
 312 into upwelling radiation leaving layer 1. These reflected photons encounter layer 1 first and last,
 313 and, possibly, layer 2 in-between. T_{12} in (76a) is the transmittance of upwelling radiation incident
 314 on the two-layer system from below. These photons encounter layer 2 first and layer 1 last.

The reflection and transmission matrices for photons incident in the opposite sense (i.e., upwelling photons from below reflected back down, and downwelling photons from above transmitted through) may be obtained by switching the indices of (74),

$$R_{12} \equiv R_2 + T_2(1 - R_1R_2)^{-1}R_1T_2 \quad (76a)$$

$$T_{21} \equiv T_2(1 - R_1R_2)^{-1}T_1 \quad (76b)$$

so that the downwelling intensity beneath the inhomogeneous two-layer system is

$$\mathbf{I}_2^- = R_{12}\mathbf{I}_2^+ + T_{21}\mathbf{I}_0^- \quad (77)$$

315 As mentioned earlier, these relations were derived for and apply to $S \times S$ -element reflection and
 316 transmission matrices that determine the S -element vectors that transform radiances incident on
 317 an inhomogeneous two-level system into exitant radiances.

We now restrict our attention to the two-stream case where all diffuse radiance is assumed to be isotropic. Since the diffuse radiance is isotropic, the reflection and transmission matrices reduce to scalar properties of each level (64)–(68). The two-stream properties of an inhomogeneous system are obtained by substituting these scalar properties for the matrices in (74)–(76). We find that an arbitrary layer 1 (or layer-combination) with scalar properties $\bar{R}_1, \bar{T}_1, \bar{R}_1, \bar{T}_1$, overlying a layer 2 (or layer-combination) with scalar properties $\bar{R}_2, \bar{T}_2, \bar{R}_2, \bar{T}_2$, behaves, as a system, with scalar optical properties. The combined reflectance and transmittance of the two-layer system to diffuse radiation incident from above, \bar{R}_{12} and \bar{T}_{12} , respectively, are

$$\bar{R}_{12} = \bar{R}_1 + \frac{\bar{T}_1\bar{R}_2\bar{T}_1}{1 - \bar{R}_1\bar{R}_2} \quad (78)$$

$$\bar{T}_{12} = \frac{\bar{T}_1\bar{T}_2}{1 - \bar{R}_1\bar{R}_2} \quad (79)$$

²The somewhat confusing convention of ordering the layers in reverse order from that which photons encounter them is due to *Coakley et al. (1983)*.

318 We have changed index conventions for the scalar two-stream properties. The subscripts for \bar{R}_{12}
 319 (78) are in the order that downwelling photons from above encounter layers 1 (first and last) and 2
 320 (possibly in-between). This notation for the two stream quantities agrees with *Collins et al. (2006)*
 321 and is opposite that of *Coakley et al. (1983)* which is used in (74)–(76). The index convention is,
 322 essentially, unchanged for the two-stream diffuse transmission \bar{T}_{12} (79), since \bar{T}_{12} is independent
 323 of layer-order. However, the diffuse reflectance \bar{R}_{12} (78) depends on layer-order, so one must
 324 carefully remember the index convention employed to label two-stream diffuse reflectances.

The reflectance and total transmittance of the combined system to downwelling direct-incident radiation, \dot{R}_{12} and \dot{T}_{12} , respectively, are

$$\begin{aligned}\dot{R}_{12} &= \dot{R}_1 + \frac{\bar{T}_1[(\dot{T}_1 - e^{-\tau_1^*/\mu_0})\bar{R}_2 + e^{-\tau_1^*/\mu_0}\dot{R}_2]}{1 - \bar{R}_1\bar{R}_2} \\ &= \dot{R}_1 + \frac{\bar{T}_1[(\dot{T}_1 - \dot{T}_1^\odot)\bar{R}_2 + \dot{T}_1^\odot\dot{R}_2]}{1 - \bar{R}_1\bar{R}_2}\end{aligned}\quad (80)$$

$$\begin{aligned}\dot{T}_{12} &= e^{-\tau_1^*/\mu_0}\dot{T}_2 + \frac{\bar{T}_2(\dot{T}_1 - e^{-\tau_1^*/\mu_0} + e^{-\tau_1^*/\mu_0}\dot{R}_2\bar{R}_1)}{1 - \bar{R}_1\bar{R}_2} \\ &= \dot{T}_1^\odot\dot{T}_2 + \frac{\bar{T}_2(\dot{T}_1 - \dot{T}_1^\odot + \dot{T}_1^\odot\dot{R}_2\bar{R}_1)}{1 - \bar{R}_1\bar{R}_2}\end{aligned}\quad (81)$$

325 Both \dot{R}_{12} and \dot{T}_{12} depend on layer-order. They are written in the *Collins et al. (2006)* conven-
 326 tion where the indices of the inhomogeneous combination are written in the order that photons
 327 would encounter the layers. The factor $\dot{T}_1 - e^{-\tau_1^*/\mu_0}$ is the fraction of direct-incident radiation that
 328 transforms to diffuse-exitant radiation while transiting the layer.

329 6.4 Discretization

330 We discretize the 25 mm depth sample holder onto a 32 layer stretched grid with vertical resolution
 331 ranging from 0.1 mm at the top to 2.5 mm at the bottom.

332 Table ?? shows the contribution of the sample holder bottom to the surface albedo at wave-
 333 lengths of 635, 1310, and 1550 nm for various snow densities.

7 GDZ09

334

335 Condensed text suggested for *Gallet et al. (2008)*:

Modeling snow reflectance in our system therefore requires the estimation of the amount of diffuse light hitting the snow. The photon distribution in an ideal integrating sphere evolves as a Markov process (*Pickering et al., 1993*). We adapted the simple yet accurate Markov model presented and evaluated in *Hidović-Rowe et al. (2006)* to our experimental geometry. The model assumes that the snow surface is flat and Lambertian. It also accounts for the optical baffle which blocks the detector from specular reflection (Figure 1). Adopting the terminology of *Hidović-Rowe et al. (2006)*, we can express the diffuse downwelling irradiance f_d^\downarrow as a fraction of the incident direct beam,

$$f_d^\downarrow = \frac{\dot{r}w\alpha s}{1 - (s + d) - w\alpha\{1 - [d + (1 - r)s]\}} \quad (82)$$

336 where \dot{r} is the snow reflectance to direct normal radiation, and w and r are, respectively, the
 337 reflectances of the sphere wall and the snow to isotropic illumination. The remaining parameters
 338 are the normalized surface areas of the sphere walls ($\alpha = 0.9816$), photodiode ($d = 0.000225$),
 339 and snow sample ($s = 0.01588$).

Correcting the preceding expression (82) to account for emission fractions \dot{f} and $1 - \dot{f}$ initially striking the sample (collimated photons) and the sphere walls (stray photons), respectively, yields

$$f_d^\downarrow = \frac{ws\{\dot{f}\dot{r}\alpha + [1 - (s + d)](1 - \dot{f})\}}{1 - (s + d) - w\alpha\{1 - [d + (1 - r)s]\}} \quad (83)$$

The signal expected to be measured at the photodiode is

$$m = \frac{wd\{\dot{f}\dot{r}\alpha + (1 - \dot{f})[1 - (s + d)]\}}{1 - (s + d) - w\alpha\{1 - [d + (1 - r)s]\}} \quad (84)$$

To estimate the contribution of the geometric artifact to surface albedo A_s , we modeled A_s as the sum over all snow layers of the product of two independent terms: the mean field-of-view (FOV, measured in hemispheres) subtended, and the albedo contribution A predicted by plane-parallel radiative transfer theory,

$$A_s = \sum_k \text{FOV}_k A_k \quad (85)$$

340 The snow was discretized on a 32-layer vertical grid stretching in layer thickness from 0.1 mm near
 341 the top to 2.5 mm near the bottom. On this grid, the top layer contributes about 10% to A_s .

342 For each layer, we calculated the mean solid angle of the integrating sphere subtended by each
 343 snow layer. Snow farther from the central axis of the sample container subtends a smaller planar
 344 angle ψ of the aperture (Figure 3), and occupies a greater relative surface area, than snow nearer
 345 the central axis. The average layer FOV is estimated as the surface-area mean FOV of all snow
 346 extending out to the radius of illumination. Note that the FOV determined in this way is geometric
 347 only; it does not account for attenuation and scattering. The FOV of diffusely illuminated snow
 348 decreases from 1.0 to 0.43 to 0.2 hemispheres as snow depth increases from 0 to 13 to 25 mm. At

349 25 mm depth, the mean FOV for snow illuminated by the collimated beam (~ 1.0 cm diameter)
350 exceeds that of snow diffusely illuminated across the entire aperture by about 6%.

351 The plane-parallel prediction of each layer's contribution to albedo A_k (85) was constructed by
352 applying the adding method to the delta-Eddington approximation of snow sample optical prop-
353 erties. After first discretizing the (presumably) homogeneous snow sample into 32 layers, the
354 procedure of *Coakley et al. (1983)* was used to determine and add the optical properties for each
355 layer. We treat the sample holder bottom as an additional layer with reflectance 6% and trans-
356 mittance 0% in order to determine its contribution to albedo. At 1310 nm, the surface albedo
357 in the 13 mm sample-holder is within about 2.5% of its semi-infinite value for fresh new snow
358 of low density (density = 50 kg m^{-3} , SSA = $1000 \text{ m}^2 \text{ kg}^{-1}$). For fresh snow of higher density
359 ($> 100 \text{ kg m}^{-3}$), or for the 25 mm sample-holder, A_s deviates from A_∞ by $< 0.1\%$. For instance,
360 this method estimates that the absorbing lower boundary reduces the measured reflectance of the
361 samples in Table 1 by from their semi-infinite value

362 The geometric correction (85) reduces the plane-parallel modeled albedo A_s for shown in Ta-
363 ble 1 by 4.3%, 4.5%, 4.7%, 1.7%, and 2.3%, respectively. This correction reduces the bias
364 between the measured and plane-parallel modeled reflectances in Table 1 by 25–50%. Hence this
365 geometric correction reduces the maximum discrepancy between our measurements and plane-
366 parallel geometry from 12% to 7%. At the same time, the geometric correction reduces A_s by less
367 than $\sim 1\%$ for denser snow ($> 200 \text{ kg m}^{-3}$) with moderate SSA ($\sim 66 \text{ m}^2 \text{ kg}^{-1}$).

368 *Text for conclusions?:* The finite horizontal and vertical dimensions of the sample perturb the
369 snow albedo from its semi-infinite, plane-parallel value. This correction can be approximated (85)
370 in terms of the layer-dependent field-of-view and the corresponding plane-parallel layer albedo
371 contribution. These factors are intuitive and predictable for all wavelengths with standard methods.
372 This geometric correction agrees well (fxm—Ghislain?) with 3D-ray tracing simulations of the
373 integrating sphere geometry.

Table 2: Notation

Sym.	Description	Value/Units
0	Zero matrix	fraction
1	Identity matrix	fraction
α	Normalized wall area	0.98114
α	Intermediate term in two-stream solution	fraction
β	Matrix diagonalization factor	fraction
γ	Intermediate term in two-stream solution	fraction
λ	Intermediate term in two-stream solution	fraction
μ_0	Cosine solar zenith angle	fraction
τ_e	Extinction optical depth	fraction
τ_e^*	Scaled extinction optical depth	fraction
ϕ	Azimuthal angle	radian
ψ	Planar angle subtended from point by aperture	radian
$\bar{\psi}$	Mean planar angle subtended from point	radian
$\bar{\bar{\psi}}$	Mean planar angle subtended by entire aperture	radian
Ω	Solid angle subtended from point to aperture	steradian
$\bar{\Omega}^d$	Mean solid angle subtended by diffusely illuminated aperture	steradian
$\bar{\Omega}^\odot$	Mean solid angle subtended by directly illuminated aperture	steradian
ϖ	Single scattering albedo	fraction
ϖ^*	Scaled single scattering albedo	fraction
AD	State: Absorbed by detector	none
AS	State: Absorbed by sample	none
AH	State: Absorbed by hole	none
AW	State: Absorbed by wall	none
C	Integration constant	none
d	Normalized detector area	0.0009

Table 2: (continued)

Sym.	Description	Value/Units
\tilde{f}_d^\downarrow	Diffuse downwelling re-illumination from “stray light”	
\tilde{f}	Fraction radiation emitted as diffuse “stray light”	
\dot{f}	Fraction radiation emitted as direct, collimated light	
f_d^\downarrow	Fraction diffuse downwelling radiation	fraction
f_{RS}^\uparrow	Fraction radiation backscattered into state RS	fraction
f_{RW}^\uparrow	Fraction radiation backscattered into state RW	fraction
f	Fraction scattered into delta-peak	fraction
g	Asymmetry parameter	fraction
g^*	Scaled asymmetry parameter	fraction
h	Normalized hole (laser source) area	0.00234
I	Identity matrix	fraction
I^+	Upwelling intensity vector	$\text{W m}^{-2} \text{Hz}^{-1} \text{sr}^{-1}$
I^-	Downwelling intensity vector	$\text{W m}^{-2} \text{Hz}^{-1} \text{sr}^{-1}$
k	Layer index	number
l	Number of reflecting states	number
m	Number of absorbing states	number
N	Number of layers	number
N	Intermediate term in two-stream solution	fraction
n	Number of total states	number
P	Transition matrix	fraction
Q	Fundamental matrix	fraction
R	Markov Reflection→Absorption matrix	fraction
R	Layer reflection matrix	fraction
R	Radius of illumination	cm
R_b	Collimated beam radius	0.5 cm
R_d	Detector radius	0.457 cm

Table 2: (continued)

Sym.	Description	Value/Units
R_e	Sample-holder radius	3.165 cm
R_s	Sample-aperture radius	1.9 cm
R_h	Laser diode radius	0.736 cm
R_{IS}	Integrating sphere radius	7.62 cm
\bar{R}	Reflectance to diffuse radiation	fraction
\dot{R}	Reflectance to direct radiation	fraction
\bar{R}_{12}	Reflectance of combined layers 1 over 2 to isotropic radiation incident from above	fraction
\dot{R}_{12}	Reflectance of combined layers 1 over 2 to direct radiation incident from above	fraction
RS	State: Reflected from sample	none
RW	State: Reflected from wall	none
r	Sample diffuse reflectance	fraction
\dot{r}	Sample direct reflectance	fraction
S	Number of radiance streams	number
s	Normalized sample area	0.0156
T	Markov Reflection→Reflection matrix	fraction
T	Layer transmission matrix	fraction
\dot{T}^\odot	Direct-beam transmittance	fraction
\bar{T}	Transmittance to diffuse radiation	fraction
\bar{T}_{12}	Transmittance of combined layers 1 over 2 to isotropic radiation incident from above	fraction
\dot{T}	Total transmittance to direct radiation	fraction
\dot{T}_{12}	Total transmittance of combined layers 1 over 2 to direct radiation incident from above	fraction
u	Intermediate term in two-stream solution	fraction
w	Wall reflectance	0.985
x	Dummy variable for integration	none

375 **Acknowledgments**

376 Supported by NSF ARC-0714088 and NASA NNX07AR23G. We thank T. Grenfell, J.-L. Jaf-
377 frezo, T. Kirchstetter, and S. Warren. Download this manuscript from [http://dust.ess.uci.edu/ppr/-](http://dust.ess.uci.edu/ppr/-ppr_ZGD09.pdf)
378 [ppr_ZGD09.pdf](http://dust.ess.uci.edu/ppr/-ppr_ZGD09.pdf).

379 **References**

- 380 Bond, T. C., and R. W. Bergstrom (2005), Light absorption by carbonaceous particles: An inves-
381 tigative review, *Aerosol Sci. Technol.*, *40*(1), 27–67, doi:10.1080/02786820500421,521. [1](#), [2](#),
382 [2.1](#)
- 383 Bond, T. C., G. Habib, and R. W. Bergstrom (2006), Limitations in the enhancement of visi-
384 ble light absorption due to mixing state, *Submitted to J. Geophys. Res.*, *111*(D20), D20,211,
385 doi:10.1029/2006JD007,315. [2.1](#)
- 386 Chang, H., and T. T. Charalampopoulos (1990), Determination of the wavelength dependence of
387 refractive indices of flame soot, *Proc. Roy. Soc. London A, Math. and Phys. Sci.*, *430*(1880),
388 577–591. [2.1](#)
- 389 Chýlek, P., V. Ramaswamy, and V. Srivastava (1983), Albedo of soot-contaminated snow, *J. Geo-*
390 *phys. Res.*, *88*, 10,837–10,843. [1](#)
- 391 Clarke, A. D., and K. J. Noone (1985), Soot in the Arctic snowpack: A cause for perturbations in
392 radiative transfer, *Atmos. Env.*, *19*(12), 2045–2053. [2](#)
- 393 Clarke, A. D., et al. (2004), Size distributions and mixtures of dust and black carbon aerosol
394 in Asian outflow: Physiochemistry and optical properties, *J. Geophys. Res.*, *109*(D15S09),
395 doi:10.1029/2003JD004,378. [2](#)
- 396 Coakley, J. A., Jr., R. D. Cess, and F. B. Yurevich (1983), The effect of tropospheric aerosols on the
397 Earth’s radiation budget: A parameterization for climate models, *J. Atmos. Sci.*, *40*, 116–138.
398 [6.3](#), [1](#), [6.3](#), [2](#), [6.3](#), [7](#)
- 399 Collins, W. D., et al. (2006), The formulation and atmospheric simulation of the Community At-
400 mosphere Model: CAM3, *J. Climate*, *19*(11), 2144–2161, doi:10.1175/JCLI3760.1. [1](#), [6.3](#), [6.3](#)
- 401 Domine, F., R. Salvatori, L. Legagneux, R. Salzano, M. Fily, and R. Casacchia (2006), Correlation
402 between the specific surface area and the short wave infrared (SWIR) reflectance of snow, *Cold*
403 *Reg. Sci. Tech.*, *46*, 60–68, doi:10.1016/j.coldregions.2006.06.002. [2.1](#)
- 404 Flanner, M. G., and C. S. Zender (2006), Linking snowpack microphysics and albedo evolution,
405 *J. Geophys. Res.*, *111*(D12), D12,208, doi:10.1029/2004GL022,076. [2.1](#)
- 406 Flanner, M. G., C. S. Zender, J. T. Randerson, and P. J. Rasch (2007), Present-day cli-
407 mate forcing and response from black carbon in snow, *J. Geophys. Res.*, *112*, D11,202,
408 doi:10.1029/2006JD008,003. [1](#), [2.1](#)

- 409 Gallet, J.-C., F. Dominé, C. S. Zender, and G. Picard (2008), Rapid and accurate measurement of
410 the specific surface area of snow using infrared reflectance at 1310 and 1550 nm, *Submitted to*
411 *The Cryosphere*. [2](#), [2.1](#), [7](#)
- 412 Grenfell, T. C., and S. G. Warren (1999), Representation of a nonspherical ice particle by a col-
413 lection of independent spheres for scattering and absorption of radiation, *J. Geophys. Res.*,
414 *104(D24)*, 31,697–31,709. [1](#), [2.1](#)
- 415 Grenfell, T. C., S. G. Warren, and P. C. Mullen (1994), Reflection of solar radiation by the Antarctic
416 snow surface at ultraviolet, visible, and near-infrared wavelengths, *J. Geophys. Res.*, *99(D9)*,
417 16,669–18,684. [1](#)
- 418 Hansen, J., and L. Nazarenko (2004), Soot climate forcing via snow and ice albedos, *Proc. Natl.*
419 *Acad. Sci.*, *101(2)*, 423–428. [1](#)
- 420 Hidović-Rowe, D., J. E. Rowe, and M. Lualdi (2006), Markov models of integrating spheres for
421 hyperspectral imaging, *Appl. Opt.*, *45(21)*, 5248–5257. [6.2](#), [6.2](#), [6.2](#), [7](#)
- 422 Hunt, G. E. (1971), A review of computational techniques for analysing the transfer of radiation
423 through a model cloudy atmosphere, *J. Quant. Spectrosc. Radiat. Transfer*, *11(6)*, 655–690,
424 doi:10.1016/0022-4073(71)90,046-X. [6.3](#)
- 425 Jacobson, M. Z. (2004), The climate response of fossil-fuel and biofuel soot, accounting for
426 soot’s feedback to snow and sea ice albedo and emissivity, *J. Geophys. Res.*, *109*, D21,201,
427 doi:10.1029/2004JD004,945. [1](#), [4](#)
- 428 Joseph, J. H., W. J. Wiscombe, and J. A. Weinman (1976), The delta-Eddington approximation for
429 radiative flux transfer, *J. Atmos. Sci.*, *33(12)*, 2452–2459. [6.3](#), [6.3](#), [6.3](#)
- 430 Krinner, G., O. Boucher, and Y. Balkanski (2006), Ice-free glacial northern Asia due to dust depo-
431 sition on snow, *Clim. Dyn.*, *27*, 613–625, doi:10.1007/s00,382-006-0159-z. [1](#)
- 432 Munneke, P. K., C. H. Reijmer, M. R. van den Broeke, G. König-Langlo, P. Stammes, and W. H.
433 Knap (2008), Analysis of clear-sky Antarctic snow albedo using observations and radiative
434 transfer modeling, *In Press in J. Geophys. Res.*, p. doi:10.1029/2007JD009653. [1](#)
- 435 Noone, K. J., and A. D. Clarke (1988), Soot scavenging measurements in Arctic snowfall, *Atmos.*
436 *Env.*, *22(12)*, 2773–2778. [1](#)
- 437 Painter, T. H., N. P. Molotch, M. Cassidy, M. Flanner, and K. Steffen (2007), Contact spectroscopy
438 for determination of stratigraphy of optical grain size, *J. Glaciol.*, *53(180)*, 121–127. [1](#)
- 439 Picard, G., L. Arnaud, F. Domine, and M. Fily (2008), Determining snow specific surface area
440 from near-infrared reflectance measurements: numerical study of the influence of grain shape,
441 *Submitted to Cold Reg. Sci. Technol.* [2](#)
- 442 Pickering, J. W., S. A. Prahl, N. van Wieringen, J. F. Beek, H. J. C. M. Sterenborg, and M. J. C. van
443 Gemert (1993), Double-integrating-sphere system for measuring the optical properties of tissue,
444 *Appl. Opt.*, *32(4)*, 399–410. [7](#)

- 445 Quinn, P. K., et al. (2008), Short-lived pollutants in the Arctic: Their climate impact and possible
446 mitigation strategies, *Atmos. Chem. Phys.*, 8, 1723–1735. [1](#)
- 447 Stamnes, K., S.-C. Tsay, W. Wiscombe, and K. Jayaweera (1988), Numerically stable algorithm
448 for discrete-ordinate-method radiative transfer in multiple scattering and emitting layered media,
449 *Appl. Opt.*, 27(12), 2502–2509. [2.1](#), [6.3](#)
- 450 Warren, S. G. (1982), Optical properties of snow, *Rev. Geophys.*, 20(1), 67–89. [1](#)
- 451 Warren, S. G. (1984), Impurities in snow: effects on albedo and snowmelt, *Annals of Glaciology*,
452 5, 177–179. [1](#)
- 453 Warren, S. G., and R. E. Brandt (2008), Optical constants of ice from the ultraviolet to the mi-
454 crowave: A revised compilation, *In Press in J. Geophys. Res.* [2.1](#)
- 455 Warren, S. G., and A. D. Clarke (1990), Soot in the atmosphere and snow surface of Antarctica,
456 *J. Geophys. Res.*, 95, 1811–1816. [1](#), [2](#)
- 457 Warren, S. G., and W. J. Wiscombe (1980), A model for the spectral albedo of snow. II: Snow
458 containing atmospheric aerosols, *J. Atmos. Sci.*, 37, 2734–2745. [1](#), [6.2](#), [6.3](#)
- 459 Watson, A. Y., and P. A. Valberg (2001), Carbon black and soot: Two different substances, *Am. Ind.*
460 *Hyg. Assoc. J.*, 62, 218–228. [2](#)
- 461 Wiscombe, W. (1977), *The Delta-Eddington Approximation for a Vertically Inhomogeneous At-*
462 *mosphere*, NCAR Tech. Note NCAR/TN–121+STR, 108 pp., National Center for Atmospheric
463 Research, Boulder, Colo. [6.3](#)
- 464 Wiscombe, W. J., and S. G. Warren (1980), A model for the spectral albedo of snow. I: Pure snow,
465 *J. Atmos. Sci.*, 37, 2712–2733. [2](#)
- 466 Wolfram Research, I. (2008), *Mathematica*, Wolfram Research, Inc., Champaign, Illinois. [6.1](#)
- 467 Zender, C. S. (1999), Global climatology of abundance and solar absorption of oxygen collision
468 complexes, *J. Geophys. Res.*, 104(D20), 24,471–24,484. [2.1](#)
- 469 Zender, C. S., and J. Talamantes (2006), Solar absorption by Mie resonances in cloud droplets,
470 *J. Quant. Spectrosc. Radiat. Transfer*, 98(1), 122–129, doi:10.1016/j.jqsrt.2005.05.084. [2.1](#)
- 471 Zender, C. S., B. Bush, S. K. Pope, A. Bucholtz, W. D. Collins, J. T. Kiehl, F. P. J. Valero,
472 and J. Vitko, Jr. (1997), Atmospheric absorption during the Atmospheric Radiation Measure-
473 ment (ARM) Enhanced Shortwave Experiment (ARESE), *J. Geophys. Res.*, 102(D25), 29,901–
474 29,915. [2.1](#)